Spatio-Temporal Electron Propagation Dynamics in Au/Fe/MgO(001) in Nonequilibrium: Revealing Single Scattering Events and the Ballistic Limit

Markus Heckschen[1,*] Yasin Beyazit,[1] Elaheh Shomali,[1] Florian Kühne,[1] Jesumony Jayabalan,[1]
Ping Zhou,[1] Detlef Diesing,[2] Markus E. Gruner,[1] Rossitza Pentcheva,[1] Axel Lorke,[1]
Björn Sothmann,[1] and Uwe Bovensiepen[1,3]

[1]*Fakultät für Physik, Universität Duisburg-Essen and CENIDE, Duisburg D-47048, Germany*

[2]*Fakultät für Chemie, Universität Duisburg-Essen and CENIDE, Essen D-45711, Germany*

[3]*Institute for Solid State Physics, The University of Tokyo, Kashiwa, Chiba 277-8581, Japan*

Understanding the microscopic spatio-temporal dynamics of nonequilibrium charge carriers in heterosystems promises optimization of process and device design towards desired energy transfer. Hot electron transport is governed by scattering with other electrons, defects, and bosonic excitations. Analysis of the energy dependence of scattering pathways and identification of diffusive, superdiffusive, and ballistic transport regimes are current challenges. Beyond our previous studies on the Au/Fe(001) heterostructure, in this work, we determine the energy-dependent change of the electron propagation time through epitaxial Au/Fe(001) heterostructures as a function of Au layer thickness. We do so by employing femtosecond time-resolved two-photon photoelectron emission spectroscopy for energies of 0.5–2.0 eV above the Fermi energy. We describe the laser-induced nonequilibrium electron excitation and injection across the Fe/Au interface using real-time time-dependent density functional theory and analyze electron propagation through the Au layer by microscopic electron transport simulations. We identify ballistic transport of minority electrons at energies with a nascent optically excited electron population, which is determined by the combination of photon energy and the specific electronic structure of the material. At lower energy, superdiffusive transport with 1–4 scattering events dominates. The effective electron velocity accelerates from 0.3 to 1 nm/fs with an increase in the Au layer thickness from 10 to 100 nm. This phenomenon is explained by electron transport that becomes preferentially aligned with the interface normal for thicker Au layers, which facilitates electron momentum or energy selection by choice of the propagation layer thickness.

I. INTRODUCTION

Optically excited processes are widely used in energy conversion applications. In photovoltaic devices, electron-hole pairs, which are excited by photon absorption, are spatially separated to induce a voltage. To increase the photovoltaic efficiency, conversion of a single photon into more than one electron-hole pair by carrier multiplication is widely discussed [1,2]. A similar issue appears in photocatalysis and photolytic water splitting [2]. An essential aspect is that optical excitations lead to nonequilibrium phenomena. On one hand, these conditions allow for carrier multiplication by carrier-carrier scattering, since the photon energy, $h\nu$, of the optical excitation is larger than the energy gap in the electronic structure. On the other hand, nonequilibrium conditions challenge our understanding of steady-state operation. An understanding of the microscopic spatio-temporal dynamics of carrier-carrier scattering, in which transport of excited carriers and their scattering with other charge carriers proceed simultaneously [3], is therefore of great interest for improved energy-related applications. Properties like the ballistic mean free path of optically excited carriers can be measured in thin films by pump-probe experiments when the pump and the probe step are spatially separated [4].

A related problem occurs in photoinduced switching of magnetization in spin valves, by femtosecond laser pulses, that aims to reduce energy consumption in data storage technology [5]. The magnetic moment of a ferromagnet can be spatially redistributed in superdiffusive

*markus.heckschen@uni-due.de

spin transport of optically excited carriers across interfaces [6,7]. Thereby, a spin-transfer torque can be induced [8], which may lead to magnetization reversal [5] at reduced energy compared to thermodynamic magnetization reversal. Furthermore, the combination of electronic excitations of layered systems has further potential regarding terahertz (THz) radiation generation [9]. In such systems, electronic excitations, which are induced optically in a ferromagnetic layer, the emitter, are transferred across an interface to another layer, the collector, which is electronically strongly interacting with the initially excited layer. For such phenomena, the energy-dependent scattering rate and length of optically excited carriers in heterosystems are essential because they determine the energy and momentum redistribution in these structures and have an impact on carrier multiplication.

Figure 1 depicts ballistic, superdiffusive, and diffusive transport regimes for an electron that is injected across an interface between an emitter and a propagation layer. For ballistic propagation, the electron passes across the layer at constant initial energy and momentum without scattering. In the superdiffusive regime, a small number of scattering events occur during electron propagation with corresponding energy and momentum changes. The secondary electrons generated in electron-electron scattering, which ensure energy and momentum conservation, are not indicated in Fig. 1. In the diffusive regime, a very large number of scattering events occur. Following Brownian motion, the variance of a single particle distribution in space grows during thermal diffusion linearly with time, whereas, in the ballistic regime, it is the traveled distance that grows linearly with time. Both regimes are bridged by superdiffusion, in which the anomalous diffusion coefficient changes between 1 and 2 in a time-dependent fashion [10]. Although Fig. 1 suggests that with increasing thickness, d, the transport regime changes from ballistic to diffusive, this is not the full picture, and a more detailed analysis is required. In the ballistic regime, the maximum angle, θ, with respect to the interface normal of the propagating electron is determined by $d = l\cos\theta$, where l is the distance between two scattering events. Accordingly, it is the angular distribution of the propagating electrons rather than d that is essential for the transport regime. For a microscopic understanding of transport phenomena, an analysis of the number of scattering events of electrons at energy E and their angular distribution under optically excited nonequilibrium conditions is desired.

In several previous studies, we established the epitaxial Au/Fe/MgO(001) heterostructure as an ideal material system to analyze ultrafast transport phenomena of optically excited electrons and spins [7,8,11–14]. In this work, we analyze the electron-propagation dynamics of optically excited electrons in the time domain by combining *ab initio* electronic structure theory in the real-time domain and microscopic transport simulations with femtosecond
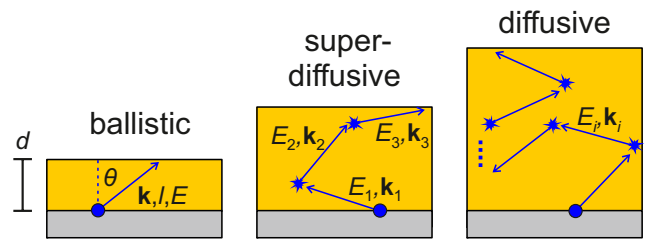

FIG. 1. Schematic electron scattering trajectories for ballistic, superdiffusive, and diffusive transport regimes in a heterostructure with an injection layer in gray and a propagation layer in yellow. Thickness of the latter is termed d. Here, E is the electron energy, $\hbar\mathbf{k}$ is the electron momentum with an injection angle θ, and l is the length between two scattering events.

time-resolved two-photon photoelectron emission spectroscopy (TR 2PPE). The Fe/Au heterostructure is considered here as a model system that facilitates achieving microscopic insights by avoiding complications, e.g., due to defect-induced scattering. As such, our work provides a fundamental understanding of the microscopic mechanisms in nonequilibrium electron transport for a metallic heterostructure. We quantify the number of scattering events and determine the angular distribution of scattered and ballistically propagating electrons.

Excitations in solids in which electrons interact with, e.g., other electrons, the crystal lattice, and/or an ordered spin system, can be represented in the electronic band structure by considering energy and momentum exchange among the corresponding degrees of freedom. Measurements of charge transport properties as a function of temperature, T, have been a leading approach to analyze these interaction processes in case of their thermal excitation. The introduction of pump-probe experiments using femtosecond laser pulses in transport studies [15] was an important step to measure the propagation dynamics of excitations in a time-of-flight-like method, but the direct study of the actual scattering pathway remained a challenge. More recent femtosecond work assigned an oscillatory time-dependent response to the superposition of three ballistic contributions in momentum space close the Fermi energy [16], where the inelastic electronic scattering times are the longest according to the Fermi liquid theory.

Au/Fe/MgO(001) is a very well controlled epitaxial heterostructure [7,17,18] with atomically sharp interfaces. We use femtosecond TR 2PPE [19–21] as a pump-probe experiment. Following our recent development [12,14], pump and probe are spatially separated on opposite sides of the heterostructure to measure the effective velocity in electronic transport as a function of electron energy above the Fermi energy, $E - E_F$, and Au layer thickness, d_{Au}, as shown schematically in Fig. 2. Due to the detailed microscopic information that we showcase here,
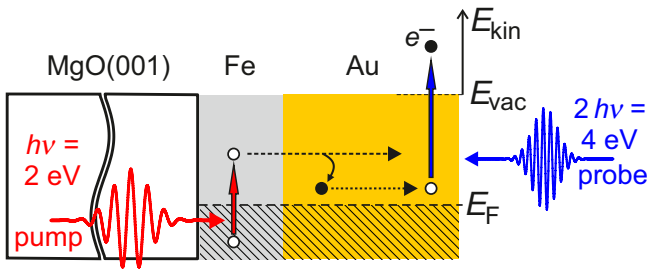
FIG. 2. Schematic of TR 2PPE spectroscopy on Au/Fe/MgO(001). Pump pulse with a photon energy of $h\nu = 2$ eV excites electrons in buried Fe at the back of the sample, which scatter during propagation through Au; these are photoemitted at the Au surface by $2h\nu = 4$ eV photons and analyzed in a spectrometer (not shown).

this approach will have an impact on transport experiments in general. Furthermore, since Fe is ferromagnetically ordered, this development is important in the field of spintronics and the spintronic THz emitters mentioned above [9]. In comparison to previous work on spin currents [7,22,23] and spin filter effects [11,24], our spectroscopic technique provides energy- and angle-dependent information. The pump-probe measurements are complemented by material-specific static and real-time (RT) time-dependent density functional theory calculations (TDDFT) that provide insights into the spin-dependent excitation pattern at the Fe/Au interface and allow us to assign the main excitation peaks observed in experiments. This is coupled with microscopic electron transport simulations to determine the relaxation and propagation pathways of electrons to the Au surface.

II. TIME-RESOLVED TWO-PHOTON PHOTOELECTRON SPECTROSCOPY

A. Sample preparation and characterization

The epitaxial Au/Fe heterostructure depicted in Fig. 2 was grown by molecular beam epitaxy on a MgO(001) substrate. The 10×10 mm^2 MgO(001) substrates (MaTeck GmbH) were cleaned in an ultrasonic bath using ethanol, isopropanol, and acetone sequentially. Carbon contamination of MgO(001) was removed in an Ar-O$_2$ atmosphere at $p = 2 \times 10^{-3}$ mbar at $T = 540$ K. Subsequently, a 7 nm film of Fe(001) was deposited at $T = 460$ K followed by deposition of Au(001) at room temperature. Pseudomorphic growth is facilitated by minimizing the lattice mismatch between MgO(001), Fe(001), and Au(001) through an in-plane rotation of the unit cells by $\pi/4$ such that MgO[010] is parallel to Fe[110], which is parallel to Au[010] [7,17,18]. The analyzed sample was prepared as a stepped wedge with 17 steps in Au film thickness, d_{Au}, from 5 to 105 nm. Each step is 400 μm wide to allow homogeneous pump laser excitation. The film thickness

was determined by a quartz microbalance during preparation in combination with time-of-flight secondary ion mass spectroscopy of a twin sample. Scanning transmission electron microscopy was used [7,8] to ensure an atomically sharp buried interface, which is crucial to avoid scattering at the interface [12,14].

B. Experimental setup

A schematic of the TR 2PPE spectroscopy setup is shown in Fig. 2. The pump pulses at a photon energy of $h\nu = 2$ eV were generated from a noncollinear optical parametric amplifier (NOPA, Clark-MXR) operated at 250 kHz used in previous work [25]. Further details of the time-resolved electron spectroscopy setup are available in Ref. [26]. Part of the NOPA output is frequency doubled to $2h\nu = 4$ eV using a β-BaB$_2$O$_4$ crystal to generate probe pulses. The duration of both pump and probe pulses were determined to be less than 40 fs. The pump and probe fluences on the sample are 50 and 1 μJ/cm^2, respectively. The pump pulse was made to enter through the MgO(001) substrate, which was transparent to 2 eV and incident on the Fe layer. To ensure homogeneous excitation on a single film thickness, the pump and probe beams were focused to a spot size with (140 ± 40) μm full width at half maximum (FWHM). Spatial overlap is determined by observing the optical transmission of the pump pulse to the Au surface on a very thin part of the Au layer, upon which the probe beam is overlaid onto the transmitted pump beam spot. The temporal overlap is obtained once the spatial overlap has been established by scanning the time delay until a two-photon photoemission signal correlated to two laser pulses is obtained. Iterative subsequent optimization of spatial and temporal overlap is used to maximize the signal. The angle of incidence of both the pump and probe pulses on the sample surface is 45°. The angle between the beam propagation directions of pump and probe laser pulses is 90°. The photoelectrons emitted from the sample surface are detected by a custom-built electron time-of-flight spectrometer [27] in the normal direction along z with an acceptance angle of $\pm 11°$ and analyzed regarding their kinetic energy, E_{kin}. For metallic surfaces, the maximum E_{kin}^{max} in 2PPE is determined by the work function Φ and $h\nu$ following $E_{kin}^{max} = 3h\nu - \Phi$. In the present study, the intermediate electronic state is probed by a photon with an energy of $2h\nu$, and the energy with respect to E_F is given by

$$E - E_F = E_{kin} + \Phi - 2h\nu. \tag{1}$$

Therefore, we access electron energies higher than 0.5 eV above E_F for the photon energy used and the work function of the sample. The samples were mounted in an ultrahigh vacuum chamber at a base pressure of 2×10^{-10} mbar and degassed for 24 h at 380 K, which avoided

intermixing of Fe and Au atoms at the interface. All measurements were performed at room temperature (300 K).

The fastest temporal response of highest-energy electrons observed in the 2PPE signal was fit to a pump-probe cross correlation. The time zero was assigned to the time delay of the maximum of this response. It is worth mentioning that, because of the finite travel time of electrons through the gold film, the determined time zero does not represent the temporal overlap of the two pulses at the pumped Fe layer, but the time delay at which the highest-energy electrons have traversed the sample and reached the Au surface. Note that 2PPE is surface sensitive [20] due to the nonlinear matrix element effects. A limit of the probing depth is estimated from the mean free path of the detected photoelectrons to 2 nm [28]. We are not sensitive to the absolute travel time within the Au film but to the energy-dependent variation of this propagation time, which we term t^*.

The experimental Fe-side pumping geometry ensures that the electron is optically excited in the Fe layer and propagates through the Au layer before it is detected by photoelectron emission on the Au surface; see Refs. [13,14] for further details and a comparison of the Fe-side and Au-side pumping configurations. The pronounced absorption of 2 eV pump photons in Fe compared to pronounced reflection at this photon energy of Au facilitates injection of the spatio-temporal profile of the charge current pulse upon femtosecond laser pulse absorption in the Fe layer across the Fe/Au interface into Au. The respective optical pump absorption profiles show that 94% of the pump light is absorbed in the Fe layer; see Fig. 1b of Ref. [14], which reports results for hot electron relaxation obtained under the same experimental conditions.

C. Experimental results

In TR 2PPE, analysis of the photoelectron intensity at a fixed energy, $E - E_F$, allows one to determine the electronic lifetime from the exponential temporal evolution [19,29]. This analysis was reported for Au/Fe heterostructures previously [12,14]. Here, we focus on the influence of d_{Au} on the electronic propagation through the Au layer. Figure 3 depicts the TR 2PPE intensity for the Fe-side pumping geometry as a function of energy above the Fermi energy, E_F, for selected d_{Au}. The Fe layer thickness, d_{Fe}, is kept constant at 7 nm. This value is a good compromise between the excited number of charge carriers, which increases with d_{Fe} as long as the thickness is considerably smaller than the optical absorption depth and the scattering length of a few nm, which leads to a relaxation of the optically excited charge carriers towards E_F [30]. Two spectroscopic signatures are observed as a function of $E - E_F$ and assigned to different locations of their origin based on their respective dependence on d_{Au}. The spectroscopic signature at $E - E_F = 1.7$ eV decreases in intensity

relative to the intensity maximum at 0.6 eV with increasing d_{Au}, such that, for $d_{Au} = 90$ nm, it is barely visible in Fig. 3, bottom. Time zero, $t = 0$, is determined by the time delay between the two laser pulses at which the highest-energy electrons at $E - E_F = 2.2$ eV are detected. The spectral signature at 1.7 eV also occurs at $t = 0$, as seen in Fig. 3. The physical origin of this feature is an interface state, which is assigned based on the real-time time-dependent DFT calculations presented in Sec. III. The second spectral signature at $E - E_F = 0.6$ eV near the low-energy cutoff is found to occur systematically at a later time delay, t^*, the larger d_{Au} is. Given the surface sensitivity of photoelectron spectroscopy, this behavior indicates that with larger d_{Au} the electron requires a longer time to propagate through the Au layer to the Au-vacuum interface. Following this hypothesis, we plot, as a function of d_{Au}, the time delay, t^*, at which the electrons at $E - E_F = 0.6$ eV are detected at the gold surface; see Fig. 4.

As shown by the red data points, the dependence of t^* on d_{Au} is sublinear in the investigated thickness range from 5 to 105 nm. As a consequence, the ratio of d_{Au} to t^*, which represents an effective electron velocity, v_{eff}, along the interface normal direction at $E - E_F = 0.6$ eV, increases with d_{Au}, as depicted in Fig. 4 as well. The observed dependence of $v_{eff}(d_{Au})$ follows linear behavior within the experimental error. This observation can be understood as follows; also see Fig. 4, inset, for an illustration. Upon injection across the Fe/Au interface, the electron has a wide phase space for its propagation in Au. Assuming an isotropic distribution of available momenta in Au, which is a reasonable approximation, as transport in Au is dominated by sp states in the relevant energy range and a ballistic propagation velocity, $v_F = \lambda/\tau$, electrons have an equal probability of propagating along the mean free path, λ, in all directions in Au during time τ, as sketched by the semicircle in the inset of Fig. 4. The electrons are injected with an energy of approximately 1.7 eV. Therefore, the electrons need at least one inelastic scattering event to reach an energy of 0.6 eV, which requires a path length that is, on average, at least the length of the mean free path, λ. This can be connected to the thickness of the gold layer by $d_{Au} = \lambda \cos\theta$, with θ as the minimum angle to ensure one inelastic collision.

The effective velocity, v_{eff}, which for ballistic electrons simply corresponds to the velocity component along the interface normal direction, is given by

$$v_{eff} = \frac{d_{Au}}{t^*} = \frac{d_{Au}}{t_1 - t_0} = v_F \frac{d_{Au}}{\lambda - d_{Au}}, \qquad (2)$$

where we assume that time t_0 is set by ballistic electrons propagating with $\theta = 0$ through the sample and time t_1 is the time electrons with 0.6 eV need to reach the sample surface. Additionally, we assume that all electrons propagate with the same velocity, $v_F = 1.4$ nm/fs [16,31,32], which
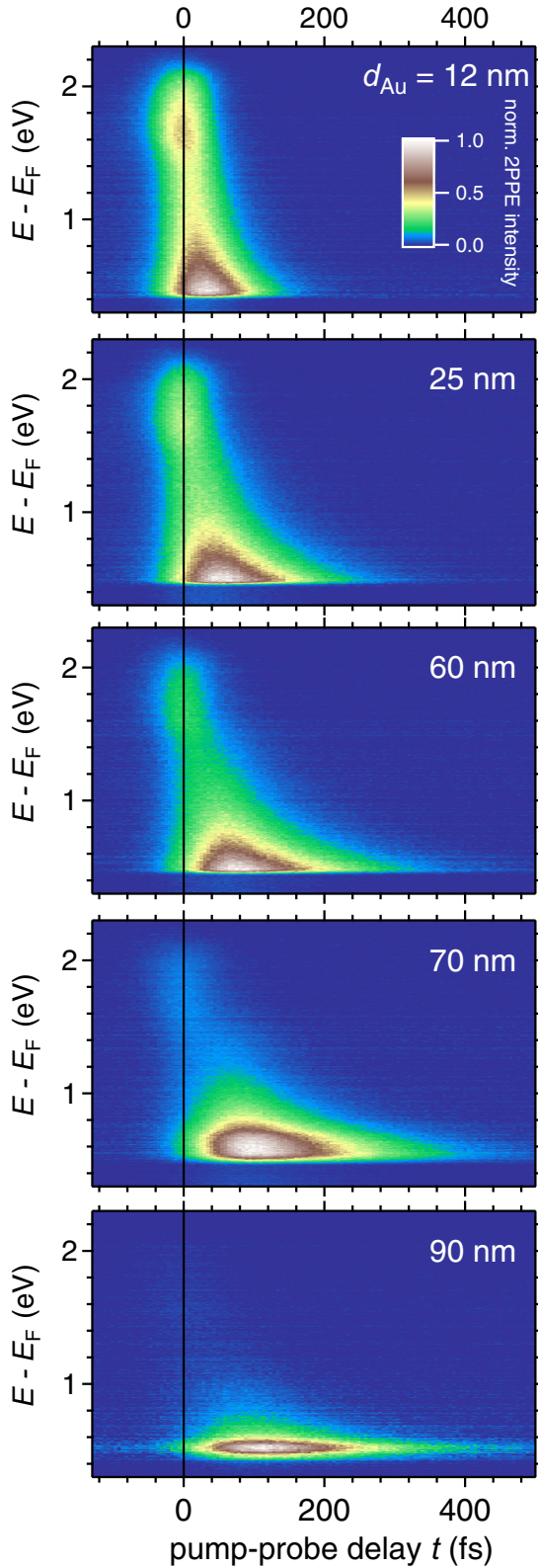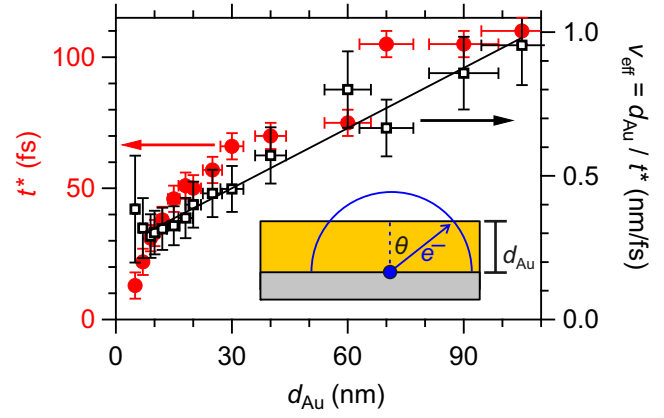
FIG. 4. Left axis (red label), time delay, t^*, due to electron propagation through Au as a function of Au layer thickness, d_{Au}, in red solid circles for the peak maximum in 2PPE intensity determined at $E - E_F = 0.6$ eV. Right axis (black label), ratio of both quantities, t^*/d_{Au}, which represents an effective electron velocity along the interface normal direction, v_{eff}, as a function of d_{Au} in black open squares. Solid line is a linear fit to the latter data. Inset illustrates the critical angle, θ, for ballistic electron propagation through the Au layer upon electron injection across the Fe/Au interface. See the text for a discussion.

is a reasonable assumption in the observed energy range [30,33]. A series expansion for small gold layer thicknesses, $d_{Au} \ll \lambda$, gives the observed linear dependence of v_{eff}:

$$v_{eff} \approx v_F \frac{d_{Au}}{\lambda} = \frac{d_{Au}}{\tau}. \tag{3}$$

A fit to the obtained linear behavior in $v_{eff}(d_{Au})$ results in $\tau = (143 \pm 10)$ fs, which is in very good agreement with literature data for inelastic hot electron lifetimes obtained by TR 2PPE [34]. Since it is unlikely that for all $\theta(d_{Au})$ a single scattering event occurs during propagation across the Au layer, we investigate various scattering pathways in simulations reported in Sec. IV. These account for the increasing width of the distribution in t for larger d_{Au} obtained in Fig. 3.

III. REAL-TIME TIME-DEPENDENT DENSITY FUNCTIONAL THEORY

To obtain a microscopic understanding of the Fe-side pump Au-side probe procedure, we carried out RT TDDFT calculations of a $Fe_5/Au_5(001)$ heterostructure excited by a laser pulse with a photon energy of $h\nu = 2$ eV, corresponding to the experimental pump pulse.

A. Method and details

The periodically repeated $Fe_5/Au_5(001)$ superlattice consists of five monolayers of bcc Fe and five monolayers of fcc Au along the (001) direction. This structure was

FIG. 3. Time-dependent 2PPE intensity as a function of energy with respect to E_F in a false color representation for different Au layer thicknesses, as indicated. Data were taken in the backside-pumping geometry, as indicated in the sketched experimental geometry. Fe layer thickness is kept constant at 7 nm.

optimized in the framework of DFT using the projected augmented wave method, as implemented in the VASP code [35,36] using the generalized gradient approximation of Perdew, Burke, and Ernzerhof [37] for the exchange cor- relation functional, a plane-wave cutoff of 450 eV, and a $15 \times 15 \times 5$ k mesh for reciprocal space sampling.

The electronic structure and TDDFT calculations in the real-time domain were performed with the full-potential linearized augmented plane-wave code ELK [38], start- ing from the previously optimized geometry. For the exchange-correlation functional, we have chosen the local spin density approximation (LSDA) in the parameteriza- tion of Perdew and Wang (PW92) [39], which shows close agreement with the VASP calculations regarding the elec- tronic structure in the static case. For heavy $5d$ elements, such as Au, accounting for spin-orbit coupling (SOC) is mandatory, as this considerably affects the ground state density of states (DOS). Thus, we include SOC in our cal- culations of the heterostructure and the respective Fe and Au bulk systems. Spin-related processes at the interface, such as spin-reorientation or spin-transfer torque, are not in the focus of our investigation. Therefore, for the sake of simplicity, we kept the spin quantization axis along the z axis, i.e., perpendicular to the interface, and initialized spin moments in this direction. In addition, to keep the numerical effort manageable, we used a plane-wave cut- off parameter, $RK_{max} = 7$, and a k-point grid of $8 \times 8 \times 3$, which proved sufficient in our previous investigations [40,41].

The RT TDDFT approach implemented in ELK prop- agates the electron density in time by integrating the time-dependent Kohn-Sham equations [42–46]. Time- dependent exchange and correlation were described within the adiabatic LSDA based on the PW92 functional. In the Kohn-Sham Hamiltonian, the electric field of the laser pulse is coupled via the corresponding vector potential to the momentum operator as a velocity gauge. As the momentum of optical photons is very small, the momenta of the excited carriers are essentially conserved, i.e., tran- sitions can be expected to take place essentially in the "vertical" direction in reciprocal space. To keep the cal- culations feasible, the simulated pulses are shorter than those in experiments. The pulse duration is limited by fold- ing the electromagnetic wave with a Gaussian envelope with a constant FWHM of 5.81 fs, which corresponds to a finite width of 0.6 eV (FWHM) in the frequency spec- trum. The maximum of the pulse with a peak power density of $S_{peak} \approx 5 \times 10^{11}$ W/cm^2 is reached at $t = 11.6$ fs after the start of the simulation. The excitation process is ana- lyzed in terms of the layer-resolved time-dependent den- sity of states, $D_\sigma(E, t)$. This quantity records the transient orbital occupation numbers, projected onto their respective energies in the static DOS [44]. It was employed recently to analyze the transient carrier dynamics of a Fe/MgO het- erostructure excited by laser pulses in the optical regime

[40,41], and allowed us to assess the relevant excitation processes and the transfer of carriers within the first 20 fs, i.e., after the laser pulse.

B. Results

The static layer- and spin-resolved DOS of the het- erostructure are shown in Fig. 5. For Fe, the majority $3d$ states are largely occupied and reach up to E_F, whereas the minority $3d$ band is partially occupied and extends up to 2.5 eV above the Fermi level. We find a sharp peak at about 1.7 eV in the central Fe layers and a somewhat smoother distribution in Fe(IF). In turn, the unoccupied majority Fe states are dominated by $4sp$ bands. The occu- pied Au $5d$ band starts 1.5 eV below E_F and shows a slight asymmetry between majority and minority spin channels, especially in the interface Au layer induced by the prox- imity to ferromagnetic Fe. Above E_F, Au $6s$ and p states prevail, exhibiting a low DOS due to the large dispersion of these bands. For a not too intense pulse, the ground state (i.e., static) DOS gives a first indication where rel- evant excitations may occur. In accordance with previous investigations [40,41], a particularly large response should be expected when either the initial or final states (or both) correspond to a region of large DOS. In the dipole approx- imation, excitations between d states are forbidden. But in transition metals, the localized d states hybridize with the states of the itinerant conduction electrons, leading to a mixture of d and sp character in the density of states of Fe. This potentially offers an increased number of ini- tial and final states for dipole-allowed optical transitions between states with p and d character, where peaks in the DOS are observed. Besides, SOC may allow for spin-flip transitions between states with equal orbital momentum as well. For the central Fe(C) layer, we find a peak in the DOS around +1.7 eV (above the Fermi level), which consists mainly of minority e_g states, with the orbital lobes ori- ented along the Cartesian axes. These can be excited from d states just below the Fermi level. States with t_{2g} char- acter form a broadened maximum around -1 eV (below E_F) and might be excited to the region around +1 eV by the laser pulse. In the majority channel, e_g states show a peak at -1 eV and might thus be involved in a transition to sp states around +1 eV, above the upper d-band edge. In Au(C), optical excitations can be expected from the upper edge of the d band at about -1.5 eV and below to sp states at about 0.5 eV above E_F.

As discussed above, the layer-resolved DOS (LDOS) of both Fe(IF) and Au(IF) are modified due to the hybridiza- tion of orbitals across the interface, which influences the transfer of excited carriers. This is further investigated in the RT TDDFT simulation. In this approach, the laser field acts on the entire heterostructure. To distinguish whether changes in occupation resulted from excitation within a specific layer in one subsystem, or whether they resulted
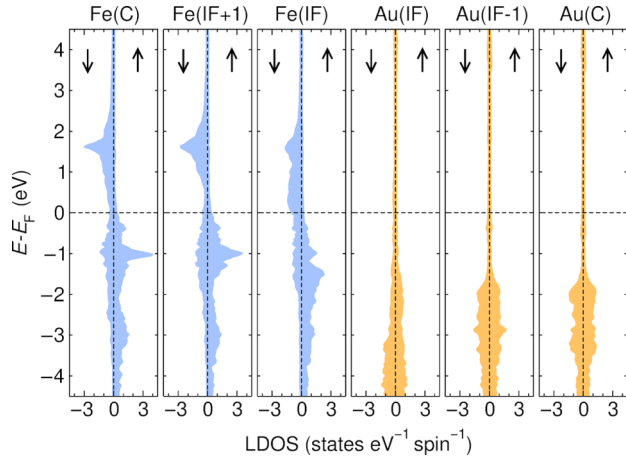
FIG. 5. Spin- and layer-resolved static DOS of the $Fe_5/Au_5(001)$ heterostructure obtained with ELK. Here, C refers to the central layers of Fe and Au, which have the largest distance from the interface layers (IF), while IF+1 and IF-1 denote the intermediate layers of Fe and Au, respectively.
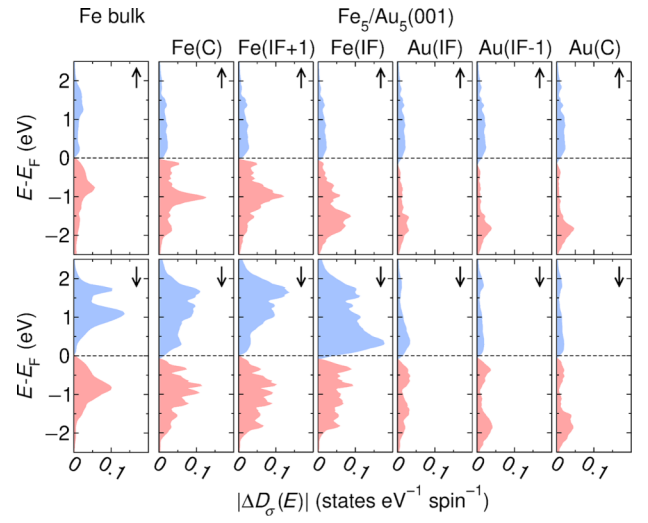

FIG. 6. Spin- and layer-resolved changes in transient occupation numbers, $\Delta D_\sigma(E) = D_\sigma(E, 20.2 \text{ fs}) - D_\sigma(E, 0)$, of the $Fe_5/Au_5(001)$ heterostructure (description of layers as in Fig. 5) and the corresponding Fe bulk material. Difference is taken between $t = 20.2$ fs after the laser pulse and $t = 0$ (before the laser pulse has been applied) for a photon energy of $h\nu = 2$ eV and linear polarization of the electric field vector along the x axis. For better visibility, we plot the absolute value of $|\Delta D_\sigma(E)|$. Blue, positive sign indicates accumulation of occupation; red, negative sign depletion of occupation. Upper panels refer to the majority spin channel and lower panels to the minority spin channel.

from (back-)propagation of carriers across the interface, we carried out additional RT TDDFT calculations of the pristine bulk systems without interfaces, i.e., ferromagnetic bcc Fe and non-spin-polarized fcc Au, which were subjected to the same laser pulse.

While the experiment is not spin-resolved, the RT TDDFT approach provides information about the particular relevance of distinct spin channels regarding the excitation process and the transfer of excited carriers [47]. The spin- and layer-resolved changes in occupation of the heterostructure and the respective bulk counterparts are displayed in Fig. 6. The plot shows the difference, $\Delta D_\sigma(E) = D_\sigma(E, 20 \text{ fs}) - D_\sigma(E, 0)$, between the transient LDOS, $D_\sigma(E, t)$, obtained for each spin orientation, σ, at $t = 20.2$ fs, right after the pulse and at $t = 0$, i.e., before the pulse has been applied. Depletion from occupied states and accumulation in unoccupied states due to laser excitation are denoted by red and blue regions, respectively.

Both for bulk Fe and the Fe layers in the heterostructure, we observe a significantly enhanced number of excited electrons in the minority channel due to the availability of unoccupied $3d$ states above E_F in contrast to the majority $3d$ states, which lie below E_F. In the minority channel of Fe(C), the excitation pattern essentially groups into three features: one at around $+1.7$ eV, one slightly above $+1$ eV, and a third smaller one at around $+0.5$ eV. Excitation at $+1.7$ eV is very pronounced in the minority spin channel of Fe bulk and the Fe layers in the heterostructure. It is not observed for bulk Au, but we find corresponding features in Au(IF), Au(IF+1), and Au(C) of the heterostructure; see Fig. 6. This means that the presence of excited carriers at this energy necessarily results from a transfer of carriers from the Fe

layers across the interface. In contrast to the first two features at $+1.7$ and $+1.0$ eV, the last one at $+0.5$ eV has no correspondence in the minority spin excitation spectrum of bulk Fe, but we find a corresponding signature in all Au layers of the heterostructure. This implies that the features around $+0.5$ eV and below in Fig. 6 essentially result from hybridization of the Fe and Au states at the interface. Nevertheless, since the Fe/Au interface is much thinner than 7 nm of bulk Fe and the pump light intensity is primarily absorbed in bulk Fe [14], we conclude that the electrons in 2PPE spectroscopy observed at $+0.6$ eV essentially result from excitations to minority spin states in Fe bulk at higher energies and are involved in scattering processes after propagating through the Fe/Au interface. This argument is supported by the experimental observation that the 2PPE intensity at $+0.6$ eV above E_F shifts to a later time delay t^* with increasing d_{Au}, while the signature in 2PPE at 1.7 eV above E_F only loses intensity with an estimated decay length of 15–20 nm in the Au layer.

IV. TRANSPORT THEORY

A. Model

In the following, we present our theoretical modeling of electron propagation in Au. We simulate classical

quasiballistic electron trajectories through a slab of thickness d_{Au} along the interface normal direction, z, and with infinite lateral extent in x and y. An electron with initial energy E is injected at $z = 0$. The initial energy is chosen randomly from a Gaussian distribution,

$$P(E) = \frac{1}{\sqrt{2\pi\sigma^2}}e^{-\frac{(E-\mu)^2}{2\sigma^2}}, \qquad (4)$$

with a mean value of $\mu = 1.7$ eV and a standard deviation of $\sigma = 0.1$ eV, in agreement with the experimental observation reported in Fig. 3 and the static and time-dependent DFT results in Figs. 5 and 6, respectively. The direction of initial electron propagation is chosen randomly with uniform angular distribution on the half-sphere indicated in Fig. 4 to ensure propagation in the positive z direction. Each electron propagates ballistically over a distance l, which is chosen randomly from the distribution

$$P(l) = \frac{1}{\lambda}e^{-l/\lambda}, \qquad (5)$$

where λ is the energy-dependent mean free path. In the experimentally relevant energy range, electrons move to a good approximation with a constant energy-independent ballistic velocity, $v_F = 1.4$ fs/nm [16,31,32], i.e., we do not have to account for band structure effects when describing electron propagation in Au. We also neglect the influence of spin-orbit coupling on transport. The ballistic velocity relates the mean free path, λ, to the electron lifetime, τ, via $\lambda = \tau v_F$ [15,33]. To get an analytical and realistic energy dependence of the electron lifetime and mean-free path, we parameterize the experimentally determined electron lifetime in gold [12,14,34] by

$$\tau = \frac{\tau_0}{1 + \left(\frac{E-E_F}{E_0}\right)^2}, \qquad (6)$$

where $\tau_0 = 170$ fs and $E_0 = 1$ eV provide a good fit to the data in the considered energy range. This approximation captures the anomaly in the lifetime of gold at $E - E_F = 1.5$ eV better than the Fermi liquid theory [34].

In our model, we assume that the electron experiences an inelastic scattering event due to electron-electron interaction after having propagated for a distance l. The scattering event has two consequences, cf. Fig. 1. First, it changes the direction of propagation. The new direction is chosen randomly and is assumed to be isotropically distributed in line with the random-k approximation [33,48]. After scattering, the electron propagates again ballistically over a new random distance l. Second, the scattering changes the electron's energy. We assume that scattering changes the energy by a random amount, ΔE, which is uniformly distributed in the interval $[0, E - E_F]$. According to Refs. [49,50], this is a reasonable assumption in the relevant

energy range. The energy, ΔE, is transferred to an electron from the Fermi sea, which, therefore, gets an energy in the range $[E_F, E_F + \Delta E]$, the trajectory of which is subsequently also included in the simulation. The secondary electron excited from the Fermi sea ensures energy and momentum conservation during the scattering process.

Electron trajectories are followed in the simulation until they reach the sample surface at $z = d_{Au}$. If the electron energy drops below a threshold value of 0.5 eV, which corresponds to the lowest energy observed in the experiment, trajectories are discarded. Furthermore, trajectories in which the electron is scattered back to the Fe/Au interface at $z = 0$ are discarded as well. In each simulation sweep, we record the total path length, which is directly linked to the propagation time, the final energy, the number of collisions along the trajectory, and the initial direction of propagation. In total, we simulated 10^7 sweeps following the propagation of the initially injected electron across the sample together with the trajectories of associated secondary electrons.

B. Results

In Fig. 7, we show the probability of electrons arriving after time t with energy $E - E_F$ at the surface for two different sample thicknesses. In analogy to the measured TR 2PPE intensity from Fig. 3, we refer to this probability as the electron intensity. For both thicknesses, $d_{Au} = 0.3\lambda_0$ and $d_{Au} = 0.6\lambda_0$ ($\lambda_0 = v_F\tau_0$), we find that a significant number of electrons arrives at the surface with their original injection energy of around 1.7 eV at time $t = d_{Au}/v_F$. This shows essentially that these electrons propagate ballistically, i.e., without any scattering through the sample in a direction close to the z axis. Here, we highlight the qualitative agreement with the measured intensities from Fig. 3. The corresponding electron intensity decays exponentially in time, cf. insets in Fig. 7, with a relaxation time that depends on energy, according to Eq. (6), following our previous results [12,14]. In principle, elastic scattering could lead to similar results. It is excluded here due to the lack of agreement between experimental and simulation results, as discussed further in Sec. V.

For thin samples, cf. main panel in Fig. 7(a), the intensity at energies below the injection energy is small. At such energies, electrons must have undergone at least one inelastic scattering process, which is unlikely for samples that are much thinner than the mean free path. In contrast, for thicker samples, as shown in the main panel of Fig. 7(b), there is significant electron intensity at low energies. Inelastic scattering events are more likely to happen in this situation because the electrons propagate a longer distance through the sample. The intensity at low energies shows a different time dependence compared to the high-energy electrons. As seen in the insets of Fig. 7 for energies $E - E_F \leq 1.5$ eV, the intensity builds up, reaches
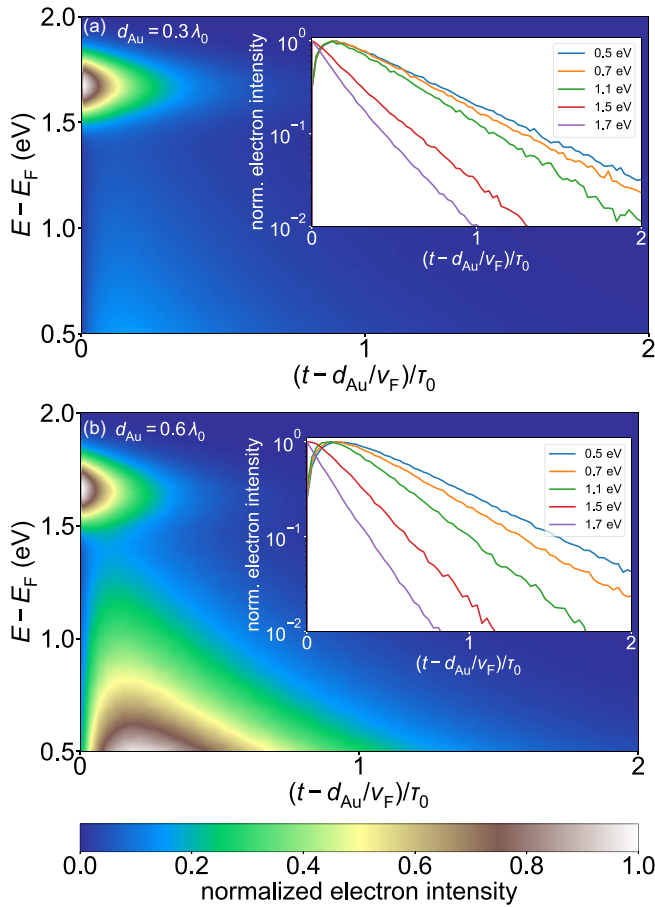
FIG. 7. Normalized electron intensity as a function of energy and time for a sample thickness of (a) $d_{Au} = 0.3\,\lambda_0$ and (b) $d_{Au} = 0.6\,\lambda_0$ in a false color representation ($\lambda_0 = v_F \tau_0$). Insets show the time evolution of electron intensity for depicted energies normalized to the maximum intensity of each energy.

a maximum (the position of which depends on the sample thickness and electron energy), and finally decays exponentially. In agreement with experimental results, we find that the most likely transit time (maxima in the insets of Fig. 7) increases sublinearly with d_{Au}, indicating that the effective electron velocity, which is defined as the ratio between the Au thickness, d_{Au}, and time delay, t^*, cf. Eq. (2), increases with increasing sample thickness.

To understand this effective acceleration of electrons, see also Fig. 4, we consider electron trajectories with a given number of inelastic scattering events separately. The time delay, t^*, between the arrival of the ballistic high-energy electrons at $t = d_{Au}/v_F$ and the maximal intensity of low-energy electrons is shown in Fig. 8 by solid lines as a function of d_{Au} for trajectories that undergo a given number of inelastic collisions. The different curves all pass through the trivial point $t^* = 0$ for $d_{Au} = 0$. For thin gold layers, t^* increases linearly with the sample thickness. For a thicker gold layer, t^* increases slower than this linear trend, i.e., it grows sublinearly. The transition between
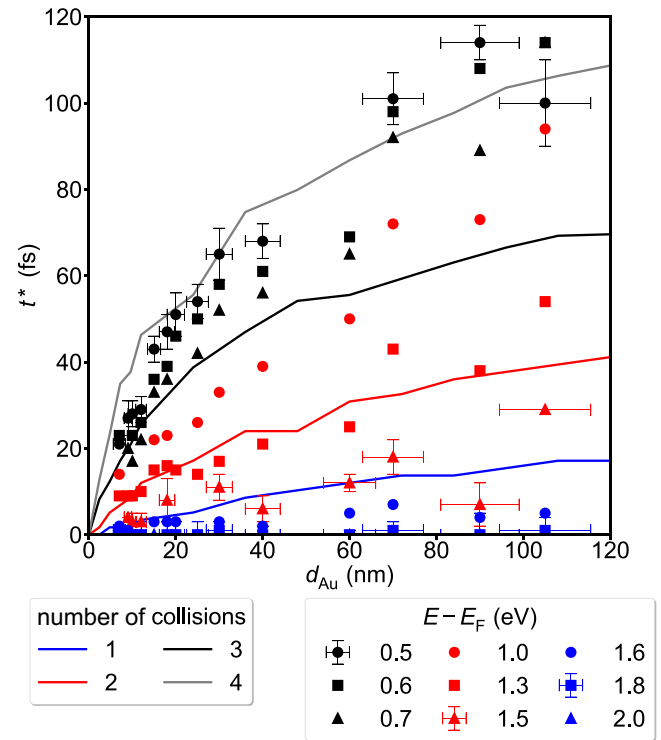

FIG. 8. Comparison of the experimentally measured time delay, t^*, for different $E - E_F$ as a function of d_{Au} and simulated trajectories with a fixed number of collisions. Simulated results are scaled to the SI unit system assuming a ballistic velocity of $v_F = 1.4\,\mathrm{nm/fs}$ and $\tau_0 = 170\,\mathrm{fs}$. For better visibility, only representative error bars are given for each group.

these two regimes occurs over a crossover range, which appears at larger d_{Au} with an increased number of inelastic scattering events. At the same time, t^* increases at a higher number of inelastic collisions. From this result, we estimate that, for collision numbers much larger than four, t^* will exhibit linear growth up to much larger gold thicknesses. Assuming that this linear behavior of t^* continues up to a very large number of collisions, we estimate the linear relationship between t^* and d_{Au} at small Au thicknesses with a propagation velocity of about 0.2 nm/fs, i.e., 7 times smaller than the Fermi velocity. In this sense, the mentioned crossover range represents the transition from a diffusive to a superdiffusive transport regime.

V. DISCUSSION

With the obtained experimental and theoretical results, we are able to provide a comprehensive microscopic picture of the optical excitation in Fe, electron injection across the interface to Au, and propagation through the Au layer. The photoinduced changes in the electronic population from the Fe bulk to the interface calculated by RT TDDFT, see Fig. 6, highlight that 2 eV photons predominantly excite minority spin electrons. These calculations

also show that the excited electronic DOS of bulk Fe are essentially recovered within 3 monolayers (ML) distance from the interface. Since one (001) atomic ML is 0.144 nm and $d_{Fe} = 7$ nm $= 49$ ML, we conclude that 2 eV photons are absorbed in Fe bulk with high probability and are, according to the population gradient across the interface, injected into the Au layer via a coherent hybrid interface state within the mean free path of Fe [30]. Direct optical excitation of such interface states plays a minor role. Near the interface, the calculated excited DOS of minority spins in Au exhibit a spectral signature with a peak at $E - E_F = 1.7$ eV and a maximum at 0.5 eV, in excellent agreement with the experimental observation in Fig. 3. This agreement confirms our description of electron injection across the interface. We note that in comparison to previous work [11], which used 1.5 eV photons and concluded injection of majority spin electrons, the RT TDDFT results indicate that the higher photon energy used here results in strong injection in the minority spin channel. This comparison is also interesting regarding minority electrons excited in Fe bulk to 1 eV above E_F. Both studies, the present one and Ref. [11], find that these excited electrons are injected with a low probability from Fe to Au.

The key experimental finding of the detection of electrons at the Au surface with a lower energy of $E - E_F = 0.5$ eV, which exhibit a time delay, t^*, compared to electron injection at 1.7 eV motivated the description of inelastically scattered electrons by microscopic transport simulations. This description agrees very well with the experimental results, cf. Figs. 3 and 7. The observation of t^* in experiments and in the transport simulations provides a direct comparison of these results, which connects the number of scattering events with the electron energy and the film thickness. Both the simulated and experimentally observed $t^*(d_{Au})$ exhibited a sublinear relationship, which was assigned to deviations from diffusive transport in Sec. IV. This consistent behavior allows one to link the electron dynamics at different energies to the number of scattering events. In Fig. 8, we depict these results by grouping the experimental data into lower (black), intermediate (red), and higher energy (blue). These groups follow the sublinear relationship. At lower energy, the corresponding t^* fall between four and three, at intermediate energy between three and one, and at higher energy below one scattering event. This last result showcases the ballistic transport regime of the primarily injected electrons for $d_{Au} < 110$ nm. The lower-energy electrons experience up to four scattering events but do not reach the diffusive regime. This finding is in agreement with our previous study, which analyzed electronic transport at lower energy near E_F in a similar experimental geometry [13] that allowed the diffusion regime to be reached. Regarding ballistic electrons, our finding differs from previous work [16], which reported ballistic contributions at particular momenta near E_F; we identified ballistic electrons

exclusively at the highest energy. Potentially, this difference originates from a different sensitivity of ballistic transport in the two different experimental methods. It is possible that the larger signal contribution of scattered electrons masks a smaller ballistic contribution, as discussed in Ref. [16].

From the above analysis, we conclude that electrons observed at energies below 1.5 eV experience at least one inelastic collision, on average. This implies that they must propagate a minimum distance of the inelastic mean free path, λ. Therefore, scattered and ballistic electrons are expected to exhibit different distributions of injection angles θ, as long as $d_{Au} < \lambda$. To confirm this, we analyze the electron momenta of the individual trajectories in our simulation. Thereby, we obtain a microscopic understanding of the transport and relaxation dynamics as well as acceleration. In Fig. 9, we show the distribution of injection angles θ for ballistic and scattered electrons for four different d_{Au}. Ballistic electrons are most likely to propagate along the interface normal direction because at $|\theta| > 0$ the pathway and scattering probability increase. The thinner the Au film, the broader the distribution of initial angles becomes. For d_{Au} close to λ_0, the angular distribution of θ for ballistic electrons becomes a narrow cone. This is in agreement with the picture discussed in the inset of Fig. 4. In contrast, scattered electrons need a path long enough to ensure at least one collision. In sufficiently thin Au films, see $d_{Au} = 0.05\lambda_0$ in Fig. 9, most electrons that scatter propagate with an initial angle close to $\theta = \pm\pi/2$, almost along the interface plane. Consequently, the effective electron velocity, $v_{eff} = d_{Au}/t^*$, to traverse the layer is much smaller than the ballistic electron velocity. Increasing the sample thickness shifts the most likely initial angle towards the interface normal direction; see Fig. 9. Hence, the effective velocity of the scattered electrons increases for larger d_{Au}, in agreement with the experimental observation in Figs. 4 and 8. This behavior suggests that momentum-dependent scattering should be applied at buried interfaces for energy selection in electron (or hole) injection across interfaces [51–53]. A potential design implies electron transmission of high-energy electrons along the interface normal and (total) reflection of electrons at larger angles, θ.

Up to now, we have only included inelastic scattering in our considerations and found the average number of inelastic collisions necessary to achieve a certain energy. We now turn to the influence of elastic scattering. Assuming an energy-independent elastic scattering time that is comparable to the inelastic lifetime of the 2.0 eV hot electrons [33], the measured apparent acceleration, i.e., the increase of v_{eff} with d_{Au}, cf. Fig. 8, would change drastically. While at 2.0 eV the ratio of elastic and inelastic scattering events would be 1:1, the ratio changes continuously to 4:1 at 0.5 eV. Hence, the total number of scattering events would be much larger than four for the low-energy
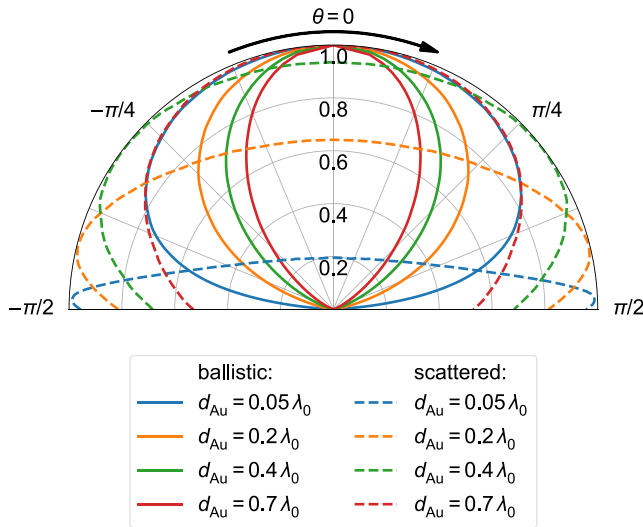
FIG. 9. Normalized angular distribution of initial polar angles for scattered and ballistic trajectories for sample thicknesses $d_{Au} = 0.05\,\lambda_0$, $0.2\,\lambda_0$, $0.4\,\lambda_0$, and $0.7\,\lambda_0$ with $\lambda_0 = v_F \tau_0$. Initial angle of $\theta = 0$ corresponds to propagation parallel to the z axis.

electrons if elastic scattering were present. In such a scenario, the time delay, t^*, of the low-energy electrons would increase linearly in Fig. 8 over the whole Au thickness range. Since the data points from the experiment are far below this limit, the experimental results indicate that the elastic scattering lifetime is much larger than the inelastic lifetime. Consequently, the elastic contributions are negligible in our analysis. Electron transport and relaxation in the optically excited nonequilibrium conditions are governed by inelastic scattering events. Recalling the single crystalline sample quality, this conclusion is in good agreement with the sample characterization available by scanning transmission electron microscopy [7,8].

Finally, we address the question of how to transfer the results reported here for Fe(100)/Au(100) to other material systems. It is obvious that defects in the propagation layer would add elastic scattering, see above, and limit ballistic propagation. This would hamper angular selection along the interface normal for ballistic electrons reported in Fig. 9. Defects at the interface, however, are potentially a very interesting modification opportunity. Since defects represent a source of momentum, the injection probability across the interface could be enhanced by lifting the requirement for injection via a coherent interface state to ensure energy and momentum conservation. One might ask how a change from metallic to semiconducting constituents affects the behavior. Essentially, we expect that the spin and angular momentum selection remain effective for semiconducting systems. The scattering probabilities would change considerably from metallic to semiconductor materials. Although impact ionization is well known for

semiconductors to be mediated by electron-electron interactions [54,55] for energies close to the conduction band minimum, electron-electron scattering plays a minor role and becomes more relevant for higher optical excitation densities, reaching a quasichemical potential in the conduction band. Under the excitation conditions investigated here, the electron-electron scattering rate in the metallic case would, more or less, be replaced by electron-phonon scattering for a semiconducting system.

VI. CONCLUSIONS

In a comprehensive experimental and theoretical study, we presented a real-time analysis of nonequilibrium optical and electronic excitations in an epitaxial Au/Fe/MgO(100) heterostructure with a focus on spatio-temporal electronic transport across the layer stack. The experimental findings are based on femtosecond time-resolved two-photon photoelectron spectroscopy, in which excitation and detection are spatially separated and confined to the Fe layer and the Au surface, respectively. Thereby, we (i) measured the energy relaxation dynamics in the transport process, and (ii) analyzed the transport mechanism microscopically. The microscopic understanding of the experimental data was rendered by two theoretical approaches. On one hand, RT TDDFT allowed us to identify the electronic states involved in excitation in the Fe part of the heterostructure and injection across the Fe/Au interface. On the other hand, this microscopic insight facilitated us to set up a transport simulation describing the propagation and relaxation processes of the hot electrons in the gold layer. The experiment revealed an effectively accelerated transport behavior with increasing Au layer thickness; this was explained in the transport simulations by an interplay of ballistic and superdiffusive trajectories with a preferential ballistic transport along the interface normal direction. The scattered electrons have a considerable planar momentum component. The electrons with highest energy propagate ballistically, while lower-energy electrons need to propagate superdiffusively to ensure relaxation beforehand.

We propose to exploit this angular-dependent transport as an energy filter to select ballistic over scattered electrons or vice versa. The microscopic and general understanding of the transport regimes and relaxation processes on the ultrafast timescale in our model system might pave the way towards an increase in energy efficiency in devices with photoexcited charge carriers, such as solar cells. Besides, our insights might be useful for understanding other phenomena related to transport in heterostructures and spin currents.

---

[1] M. A. Green, Third generation photovoltaics: Ultra-high conversion efficiency at low cost, Prog. Photovolt.: Res. Appl. **9**, 123 (2001).

[2] M. C. Hanna and A. J. Nozik, Solar conversion efficiency of photovoltaic and photoelectrolysis cells with carrier multiplication absorbers, J. Appl. Phys. **100**, 074510 (2006).

[3] S. Akel, A. Kulkarni, U. Rau, and T. Kirchartz, Relevance of long diffusion lengths for efficient halide perovskite solar cells, PRX Energy **2**, 013004 (2023).

[4] J. Sung, C. Schnedermann, L. Ni, A. Sadhanala, R. Y. S. Chen, C. Cho, L. Priest, J. M. Lim, H.-K. Kim, B. Monserrat, P. Kukura, and A. Rao, Long-range ballistic propagation of carriers in methylammonium lead iodide perovskite thin films, Nat. Phys. **16**, 171 (2020).

[5] J. Igarashi, W. Zhang, Q. Remy, E. Díaz, J.-X. Lin, J. Hohlfeld, M. Hehn, S. Mangin, J. Gorchon, and G. Malinowski, Optically induced ultrafast magnetization switching in ferromagnetic spin valves, Nat. Mater. **22**, 725 (2023).

[6] M. Battiato, K. Carva, and P. M. Oppeneer, Superdiffusive spin transport as a mechanism of ultrafast demagnetization, Phys. Rev. Lett. **105**, 027203 (2010).

[7] A. Melnikov, I. Razdolski, T. O. Wehling, E. T. Papaioannou, V. Roddatis, P. Fumagalli, O. Aktsipetrov, A. I. Lichtenstein, and U. Bovensiepen, Ultrafast transport of laser-excited spin-polarized carriers in Au/Fe/MgO(001), Phys. Rev. Lett. **107**, 076601 (2011).

[8] I. Razdolski, A. Alekhin, N. Ilin, J. P. Meyburg, V. Roddatis, D. Diesing, U. Bovensiepen, and A. Melnikov, Nanoscale interface confinement of ultrafast spin transfer torque driving non-uniform spin dynamics, Nat. Commun. **8**, 15007 (2017).

[9] T. S. Seifert, L. Cheng, Z. Wei, T. Kampfrath, and J. Qi, Spintronic sources of ultrashort terahertz electromagnetic pulses, Appl. Phys. Lett. **120**, 180401 (2022).

[10] M. Battiato, K. Carva, and P. M. Oppeneer, Theory of laser-induced ultrafast superdiffusive spin transport in layered heterostructures, Phys. Rev. B **86**, 024404 (2012).

[11] A. Alekhin, I. Razdolski, N. Ilin, J. P. Meyburg, D. Diesing, V. Roddatis, I. Rungger, M. Stamenova, S. Sanvito, U. Bovensiepen, and A. Melnikov, Femtosecond spin current pulses generated by the nonthermal spin-dependent seebeck effect and interacting with ferromagnets in spin valves, Phys. Rev. Lett. **119**, 017202 (2017).

[12] Y. Beyazit, J. Beckord, P. Zhou, J. Meyburg, F. Kühne, D. Diesing, M. Ligges, and U. Bovensiepen, Local and nonlocal electron dynamics of Au/Fe/MgO(001) heterostructures analyzed by time-resolved two-photon photoemission spectroscopy, Phys. Rev. Lett. **125**, 076803 (2020).

[13] F. Kühne, Y. Beyazit, B. Sothmann, J. Jayabalan, D. Diesing, P. Zhou, and U. Bovensiepen, Ultrafast transport and energy relaxation of hot electrons in Au/Fe/MgO(001) heterostructures analyzed by linear time-resolved photoelectron spectroscopy, Phys. Rev. Res. **4**, 033239 (2022).

[14] Y. Beyazit, F. Kühne, D. Diesing, P. Zhou, J. Jayabalan, B. Sothmann, and U. Bovensiepen, Ultrafast electron dynamics in Au/Fe/MgO(001) analyzed by Au- and Fe-selective pumping in time-resolved two-photon photoemission spectroscopy: Separation of excitations in adjacent metallic layers, Phys. Rev. B **107**, 085412 (2023).

[15] S. D. Brorson, J. G. Fujimoto, and E. P. Ippen, Femtosecond electronic heat-transport dynamics in thin gold films, Phys. Rev. Lett. **59**, 1962 (1987).

[16] X. Liu, R. Stock, and W. Rudolph, Ballistic electron transport in Au films, Phys. Rev. B **72**, 195431 (2005).

[17] T. Mühge, A. Stierle, N. Metoki, H. Zabel, and U. Pietsch, Structural properties of high-quality sputtered Fe films on Al_2O_3(1120) and MgO(001) substrates, Appl. Phys. A **59**, 659 (1994).

[18] M. Mattern, A. von Reppert, S. P. Zeuschner, J.-E. Pudell, F. Kühne, D. Diesing, M. Herzog, and M. Bargheer, Electronic energy transport in nanoscale Au/Fe heterostructures in the perspective of ultrafast lattice dynamics, Appl. Phys. Lett. **120**, 092401 (2022).

[19] H. Petek and S. Ogawa, Femtosecond time-resolved two-photon photoemission studies of electron dynamics in metals, Prog. Surf. Sci. **56**, 239 (1997).

[20] M. Weinelt, Time-resolved two-photon photoemission from metal surfaces, J. Phys.: Condens. Matter **14**, R1099 (2002).

[21] U. Bovensiepen and P. Kirchmann, Elementary relaxation processes investigated by femtosecond photoelectron spectroscopy of two-dimensional materials, Laser. Photonics Rev. **6**, 589 (2012).

[22] G. Malinowski, F. Dalla Longa, J. H. H. Rietjens, P. V. Paluskar, R. Huijink, H. J. M. Swagten, and B. Koopmans, Control of speed and efficiency of ultrafast demagnetization by direct transfer of spin angular momentum, Nat. Phys. **4**, 855 (2008).

[23] N. Bergeard, M. Hehn, S. Mangin, G. Lengaigne, F. Montaigne, M. Lalieu, B. Koopmans, and G. Malinowski, Hot-electron-induced ultrafast demagnetization in Co/Pt multilayers, Phys. Rev. Lett. **117**, 147203 (2016).

[24] A. Melnikov, L. Brandt, N. Liebing, M. Ribow, I. Mertig, and G. Woltersdorf, Ultrafast spin transport and control of spin current pulse shape in metallic multilayers, Phys. Rev. B **106**, 104417 (2022).

[25] P. Auburger, I. Kemeny, C. Bertram, M. Ligges, M. Bockstedte, U. Bovensiepen, and K. Morgenstern, Microscopic insight into electron-induced dissociation of aromatic molecules on ice, Phys. Rev. Lett. **121**, 206001 (2018).

[26] M. Sandhofer, I. Y. Sklyadneva, V. Sharma, V. M. Trontl, P. Zhou, M. Ligges, R. Heid, K. P. Bohnen, E. V. Chulkov, and U. Bovensiepen, Unoccupied electronic structure and relaxation dynamics of Pb/Si(111), J. Electron Spectros. Relat. Phenomena **195**, 278 (2014).

[27] P. Kirchmann, L. Rettig, D. Nandi, U. Lipowski, M. Wolf, and U. Bovensiepen, A time-of-flight spectrometer for angle-resolved detection of low energy electrons in two dimensions, Appl. Phys. A **91**, 211 (2008).

[28] U. Bovensiepen, Coherent and incoherent excitations of the Gd(0001) surface on ultrafast timescales, J. Phys.: Condens. Matter **19**, 083201 (2007).

[29] U. Bovensiepen, H. Petek, and M. Wolf, *Dynamics at Solid State Surfaces and Interfaces* (Wiley-VCH, Weinheim, 2010), 1st ed.

[30] V. P. Zhukov, E. V. Chulkov, and P. M. Echenique, Lifetimes and inelastic mean free path of low-energy excited electrons in Fe, Ni, Pt, and Au: *Ab initio* GW + T calculations, Phys. Rev. B **73**, 125105 (2006).

[31] J. I. Mustafa, M. Bernardi, J. B. Neaton, and S. G. Louie, *Ab initio* electronic relaxation times and transport in noble metals, Phys. Rev. B **94**, 155105 (2016).

[32] D. Gall, Electron mean free path in elemental metals, J. Appl. Phys. **119**, 085101 (2016).

[33] D. M. Nenno, B. Rethfeld, and H. C. Schneider, Particle-in-cell simulation of ultrafast hot-carrier transport in Fe/Au heterostructures, Phys. Rev. B **98**, 224416 (2018).

[34] M. Bauer, A. Marienfeld, and M. Aeschlimann, Hot electron lifetimes in metals probed by time-resolved two-photon photoemission, Prog. Surf. Sci. **90**, 319 (2015).

[35] G. Kresse and J. Furthmüller, Efficient iterative schemes for *ab initio* total-energy calculations using a plane-wave basis set, Phys. Rev. B **54**, 11169 (1996).

[36] G. Kresse and D. Joubert, From ultrasoft pseudopotentials to the projector augmented-wave method, Phys. Rev. B **59**, 1758 (1999).

[37] J. P. Perdew, K. Burke, and M. Ernzerhof, Generalized gradient approximation made simple, Phys. Rev. Lett. **77**, 3865 (1996).

[38] The Elk code, version 8.3.15, http://elk.sourceforge.net/ (2022).

[39] J. P. Perdew and Y. Wang, Accurate and simple analytic representation of the electron-gas correlation energy, Phys. Rev. B **45**, 13244 (1992).

[40] M. E. Gruner and R. Pentcheva, Dynamics of optical excitations in a Fe/MgO(001) heterostructure from time-dependent density functional theory, Phys. Rev. B **99**, 195104 (2019).

[41] E. Shomali, M. E. Gruner, and R. Pentcheva, Anisotropic carrier dynamics in a laser-excited $Fe_1/(MgO)_3(001)$ heterostructure from real-time time-dependent density functional theory, Phys. Rev. B **105**, 245103 (2022).

[42] K. Krieger, J. K. Dewhurst, P. Elliott, S. Sharma, and E. K. U. Gross, Laser-induced demagnetization at ultrashort time scales: Predictions of TDDFT, J. Chem. Theory Comput. **11**, 4870 (2015).

[43] P. Elliott, T. Müller, J. K. Dewhurst, S. Sharma, and E. K. U. Gross, Ultrafast laser induced local magnetization dynamics in Heusler compounds, Sci. Rep. **6**, 38911 (2016).

[44] J. K. Dewhurst, P. Elliott, S. Shallcross, E. K. U. Gross, and S. Sharma, Laser-induced intersite spin transfer, Nano Lett. **18**, 1842 (2018).

[45] P. Elliott, K. Krieger, J. K. Dewhurst, S. Sharma, and E. K. U. Gross, Optimal control of laser-induced spin–orbit mediated ultrafast demagnetization, New J. Phys. **18**, 013014 (2016).

[46] J. K. Dewhurst, K. Krieger, S. Sharma, and E. K. U. Gross, An efficient algorithm for time propagation as applied to linearized augmented plane wave method, Comput. Phys. Commun. **209**, 92 (2016).

[47] We observe only moderate transient changes in the magnetization of the system during and after application of the laser pulse. The total magnetization of the heterostructure is initially $13.0\,\mu_B$ oriented along the z axis and reduces by $0.63\,\mu_B$ as a function of time, while only minute x and y components in the order of $10^{-1}\,\mu_B$ appear.

[48] M. Battiato and K. Held, Ultrafast and gigantic spin injection in semiconductors, Phys. Rev. Lett. **116**, 196601 (2016).

[49] W. S. M. Werner, K. Glantschnig, and C. Ambrosch-Draxl, Optical constants and inelastic electron-scattering data for 17 elemental metals, J. Phys. Chem. Ref. Data **38**, 1013 (2009).

[50] A. Alkauskas, S. D. Schneider, C. Hébert, S. Sagmeister, and C. Draxl, Dynamic structure factors of Cu, Ag, and Au: Comparative study from first principles, Phys. Rev. B **88**, 195124 (2013).

[51] G. Binasch, P. Grünberg, F. Saurenbach, and W. Zinn, Enhanced magnetoresistance in layered magnetic structures with antiferromagnetic interlayer exchange, Phys. Rev. B **39**, 4828 (1989).

[52] P. M. Levy, S. Zhang, and A. Fert, Electrical conductivity of magnetic multilayered structures, Phys. Rev. Lett. **65**, 1643 (1990).

[53] S. Yuasa, T. Nagahama, A. Fukushima, Y. Suzuki, and K. Ando, Giant room-temperature magnetoresistance in single-crystal Fe/MgO/Fe magnetic tunnel junctions, Nat. Mater. **3**, 868 (2004).

[54] M. C. Hoffmann, J. Hebling, H. Y. Hwang, K.-L. Yeh, and K. A. Nelson, Impact ionization in InSb probed by terahertz pump—terahertz probe spectroscopy, Phys. Rev. B **79**, 161201 (2009).

[55] H. Tanimura, J. Kanasaki, and K. Tanimura, State-resolved ultrafast dynamics of impact ionization in InSb, Sci. Rep. **4**, 6849 (2014).